

Cramér-Rao Bounds for Holographic Positioning

Antonio A. D’Amico, Andrea de Jesus Torres, Luca Sanguinetti, *Senior Member, IEEE*, Moe Win, *Fellow, IEEE*

Abstract—Multiple antennas arrays play a key role in wireless networks for communications but also for localization and sensing applications. The use of large antenna arrays at high carrier frequencies (in the mmWave range) pushes towards a propagation regime in which the wavefront is no longer plane but spherical. This allows to infer the position and orientation of a transmitting source from the received signal without the need of using multiple anchor nodes, located in known positions. To understand the fundamental limits of large antenna arrays for localization, this paper combines wave propagation theory with estimation theory, and computes the Cramér-Rao Bound (CRB) for the estimation of the source position on the basis of the three Cartesian components of the electric field, observed over a rectangular surface area. The problem is referred to as holographic positioning and is formulated by taking into account the radiation angular pattern of the transmitting source, which is typically ignored in standard signal processing models. We assume that the source is a Hertzian dipole, and address the holographic positioning problem in both cases, that is, with and without a priori knowledge of its orientation. To simplify the analysis and gain further insights, we also consider the case in which the dipole is located on the line perpendicular to the surface center. Numerical and asymptotic results are given to quantify the CRBs, and to quantify the effect of various system parameters on the ultimate estimation accuracy. It turns out that surfaces of practical size may guarantee a centimeter-level accuracy in the mmWave bands.

Index Terms—Cramér-Rao bound, near field, spherical wavefront, source localization, planar electromagnetic surfaces, holographic positioning.

I. INTRODUCTION

The estimation accuracy of signal processing algorithms for positioning is fundamentally limited by the quality of the underlying measurements. For time-based measurements, high resolution and high accuracy can only be obtained when a large bandwidth is available. Improvements can be achieved by using multiple anchor nodes, located in known positions. Antenna arrays have thus far only played a marginal role in positioning since the small arrays of today’s networks provide little benefit. With future networks, the situation may change significantly. Indeed, the 5G technology standard is envisioned to operate in bands up to 86 GHz [2], while 6G research is already focusing on the so-called sub-terahertz

(THz) bands, i.e., in the range 100 – 300 GHz. The small wavelengths of high-frequency signals make it practically possible to envision arrays with a very large number of finely tailorable antennas, as never seen before. The advent of large spatially-continuous electromagnetic surfaces interacting with wireless signals pushes even further this vision. Research in this direction is taking place under the names of Holographic MIMO [3]–[5], large intelligent surfaces [6], [7], and reconfigurable intelligent surfaces [8], [9]. All this opens new dimensions and brings new opportunities for communications but also for localization and sensing [10].

A. Motivation and contribution

A side-effect of using large arrays or surfaces combined with high carrier frequencies is to push the electromagnetic propagation towards the regime in which the wavefront associated to the signal transmitted by the source tends to be spherical and cannot be approximated by a plane wave. In this regime, also the distance information, not only the angle-of-arrival, can be inferred from it. This concept is not new [11] and it has been widely used to develop signal processing algorithms that exploit the spherical wavefront properties to communicate in low rank propagation channels (e.g., [12]–[14]) and to pinpoint the position of the source with high accuracy [7], [15]–[23]. In this latter context, the question arises of the ultimate accuracy that can be achieved in localization operations. This is important in order to provide benchmarks for evaluating the performance of actual estimators.

Motivated by this consideration, in this paper we combine electromagnetic propagation concepts with estimation theory, and compute the Cramér-Rao Bound (CRB) for source localization. In doing so, we exploit the exact expression (in the Fraunhofer radiation region of the source) of the three Cartesian components of the electric vector field, observed over a rectangular spatial region. These components depend on the radiation vector, which is in turn determined by the current distribution inside the source. This functional dependence is typically overlooked in *standard* signal processing models used for CRB computations. Despite possible, it must be clear that such approach has the following relevant shortcomings. Firstly, the CRBs computed by using approximate models that neglect relevant information about the source position are inevitably *unaccurate* to quantify the ultimate accuracy in source localization. Secondly, the true model may depend on unknown parameters (i.e., *nuisance parameters*) that, although not related to the source position, make the CRB obtained by ignoring them wrong. Note that similar considerations can be found in [11] where *standard* models are compared to the so-called *analytic models*, based on electromagnetic theory. Particularly, [11] observes that the former typically ignore the

Part of this paper was presented at the 2021 Asilomar Conference on Signals, Systems, and Computers [1].

A. A. D’Amico, A. de Jesus Torres and Luca Sanguinetti are with the Dipartimento di Ingegneria dell’Informazione, University of Pisa, Italy. (e-mail: {a.damico, luca.sanguinetti}@unipi.it, andrea.dejesustorres@phd.unipi.it).

M. Win is with the Wireless Information and Network Sciences Laboratory (WINSLab), Massachusetts Institute of Technology (MIT), Cambridge, MA 02139 USA (e-mail: moewin@mit.edu)

The research was supported by the MISTI Global Seed Funds. L. Sanguinetti and A. A. D’Amico were also partially supported by the Italian Ministry of Education and Research (MIUR) in the framework of the CrossLab project (Departments of Excellence).

nature of the source whose physical characteristics have a profound impact on the generated electromagnetic fields.

Our objective here is to provide the true signal model based on first principles in electromagnetic theory and use it to compute the CRBs for the localization of a Hertzian dipole, that has been largely considered in the literature but using *standard* models. Further simplifications and insights are obtained by assuming that the dipole is located on the line perpendicular to the surface center. To make the treatment more general, we consider a vector wave model. Note that scalar approximations are often used to simplify the analysis and provide an intermediate step toward the understanding of the vector wave model. These simplifications may simply follow from considering one of the three components of the electric field or also from using the component of the Poynting vector perpendicular (in each point) to the observation region [7]. Not relying on the above assumptions allows us to derive a more fundamental limit to the accuracy of actual estimators that may possibly exploit the entire electric field. This is called *holographic positioning* where the holographic term dates back to the ancient greek and literally means “describe everything” [5].

Compared to the conference version [1], this paper provides a more detailed derivation and discussion of the electromagnetic vector model and computes the CRBs in both cases, that is, with and without a priori knowledge of the Hertzian dipole orientation. Also, it provides all the derivations that were omitted in [1].

B. Paper outline and notation

The paper is organized as follows. In Section II, we start from first principles of wave propagation theory and provide the most general form of the electric field, which is then used to compute the CRB for the estimation of the position of the transmitting source. We also briefly describe how simplified models can be obtained from the general form. In Section III, we simplify the analysis by assuming that the transmitting source is an elementary dipole pointing in an arbitrary direction. The CRBs for the estimation of the dipole position are computed for both cases, i.e., with and without a priori knowledge of its orientation. To gain insights into the CRBs, in Section IV we assume that the dipole is located in the central perpendicular line (CPL) and is vertically oriented. Insightful closed-form expressions are provided to quantify the ultimate estimation accuracy. In Section V, we provide some numerical results as a function of system parameters, e.g., distance, array size, carrier frequency. The major conclusions are drawn in Section VI.

The following notation is used throughout the paper. In the \mathbb{R}^3 Euclidean space, an arbitrary spatial vector \mathbf{r} is represented as $\mathbf{r} = (\alpha, \beta, \gamma)$, where (α, β, γ) are the *components* of \mathbf{r} along the directions of three given orthonormal vectors $\hat{\mathbf{u}}_1, \hat{\mathbf{u}}_2, \hat{\mathbf{u}}_3$. Equivalently, we write $\mathbf{r} = \alpha\hat{\mathbf{u}}_1 + \beta\hat{\mathbf{u}}_2 + \gamma\hat{\mathbf{u}}_3$. The length of \mathbf{r} is $\|\mathbf{r}\| = \sqrt{\alpha^2 + \beta^2 + \gamma^2}$, and $\hat{\mathbf{r}} = \mathbf{r}/\|\mathbf{r}\|$ is a unit vector that is parallel to \mathbf{r} . We use $\mathbf{a} \times \mathbf{b}$ and $\mathbf{a} \cdot \mathbf{b}$ to denote, respectively, the cross and the dot product between \mathbf{a} and \mathbf{b} . An arbitrary point P in \mathbb{R}^3 is described by its three *coordinates* with respect

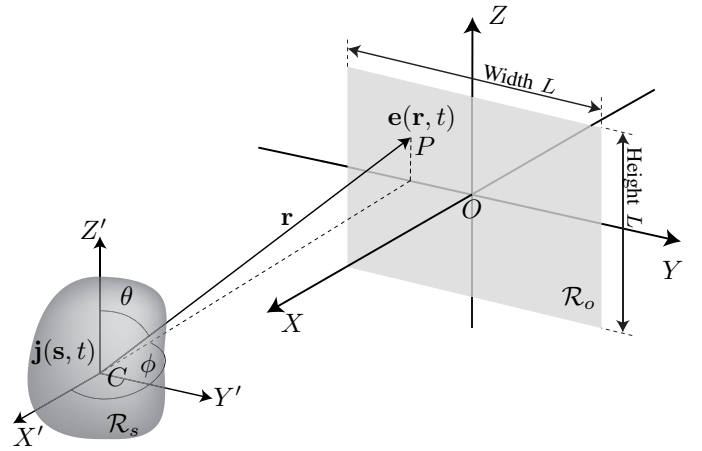


Fig. 1: Geometry of the considered system.

to a reference system (cartesian or spherical). A point P can also be represented by a vector \mathbf{r} . In such a case, P is the endpoint of \mathbf{r} , whose starting point is fixed.

C. Reproducible research

The Matlab code used to obtain the simulation results will be made available upon completion of the review process.

II. SIGNAL MODEL AND PROBLEM FORMULATION

Consider the system depicted in Fig. 1 in which an electric current density $\mathbf{j}(\mathbf{s}, t)$, inside a source region \mathcal{R}_s , generates an electric field $\mathbf{e}(\mathbf{r}, t)$ at a generic point P , identified through the spatial vector \mathbf{r} . We consider only monochromatic sources and fields of the form

$$\mathbf{j}(\mathbf{s}, t) = \text{Re} \{ \mathbf{j}(\mathbf{s}) e^{j\omega t} \} \quad (1)$$

and

$$\mathbf{e}(\mathbf{r}, t) = \text{Re} \{ \mathbf{e}(\mathbf{r}) e^{j\omega t} \}. \quad (2)$$

In this case, Maxwell's equations can be written only in terms of the current and field *phasors*, $\mathbf{j}(\mathbf{s})$ and $\mathbf{e}(\mathbf{r})$ [24, Ch. 1].

We call C the *centroid* of the source region \mathcal{R}_s and assume that the electric field $\mathbf{e}(\mathbf{r})$, produced by $\mathbf{j}(\mathbf{s})$, is measured over an *observation region* \mathcal{R}_o outside \mathcal{R}_s . The electromagnetic field propagates in a homogeneous and isotropic medium with neither obstacles nor reflecting surfaces. In other words, there is only a line-of-sight link between \mathcal{R}_s and \mathcal{R}_o .

A. Signal model

The measured field is the sum of $\mathbf{e}(\mathbf{r})$ and a random noise field $\mathbf{n}(\mathbf{r})$, i.e.,

$$\boldsymbol{\xi}(\mathbf{r}) = \mathbf{e}(\mathbf{r}) + \mathbf{n}(\mathbf{r}) \quad (3)$$

where $\mathbf{n}(\mathbf{r})$ is generated by electromagnetic sources outside \mathcal{R}_s . Consider a cartesian coordinate system $CX'Y'Z'$ with the origin in the centroid C in Fig. 1 and make the following assumption.

Assumption 1. *The observation region is a square domain parallel to the $Y'Z'$ coordinate plane. In particular, assume that*

$$\mathcal{R}_o = \{ (x', y', z') : x' = x'_o, |y' - y'_o| \leq L/2, |z' - z'_o| \leq L/2 \}$$

where (x'_o, y'_o, z'_o) are the cartesian coordinates of the center O of \mathcal{R}_o in the system $CX'Y'Z'$.

The cartesian system $OXYZ$ in Fig. 1 is obtained by $CX'Y'Z'$ through a pure translation. We denote by $\hat{\mathbf{x}}$, $\hat{\mathbf{y}}$ and $\hat{\mathbf{z}}$, the unit vectors in the $X(X')$, $Y(Y')$ and $Z(Z')$ directions, respectively. The position of C in the system $OXYZ$ is given by the cartesian coordinates (x_C, y_C, z_C) . Accordingly, we have that $x' = x - x_C$, $y' = y - y_C$ and $z' = z - z_C$. The following assumption is further made.

Assumption 2. Let r_o be the distance of C from \mathcal{R}_o and denote by l_s the largest dimension of \mathcal{R}_s . We assume that $r_o \gg l_s$ and $r_o \gg 2l_s^2/\lambda$, where $\lambda = 2\pi c/\omega$ is the wavelength. These conditions define the so-called far-field or Fraunhofer radiation region of the source [25, Ch. 15].

In the Fraunhofer radiation region of the source, the electric field $\mathbf{e}(\mathbf{r})$ can be approximated as [25, Ch. 15]:

$$\mathbf{e}(\mathbf{r}) = G(r) [\hat{\mathbf{r}} \times \mathbf{R}(\theta, \phi)] \times \hat{\mathbf{r}} \quad (4)$$

where (r, θ, ϕ) are the spherical coordinates (with respect to $CX'Y'Z'$) of a generic point $\mathbf{r} \in \mathcal{R}_o$, i.e., $\mathbf{r} = r \cos \phi \sin \theta \hat{\mathbf{x}} + r \sin \phi \sin \theta \hat{\mathbf{y}} + r \cos \theta \hat{\mathbf{z}}$, and

$$G(r) = -jkZ_0 \frac{e^{-jkr}}{4\pi r} \quad (5)$$

is the scalar Green's function with $k = 2\pi/\lambda$ being the wavenumber and Z_0 being the characteristic impedance of the medium. Also, in (4) $\hat{\mathbf{r}}$ is the unit vector in the radial direction, and $\mathbf{R}(\theta, \phi)$ is the radiation vector. The latter is related to the source current distribution $\mathbf{j}(\mathbf{s})$ by the following equation [25, Eq. (15.7.5)]

$$\mathbf{R}(\theta, \phi) = \int_{\mathcal{R}_s} \mathbf{j}(\mathbf{s}) e^{j\mathbf{k}(\theta, \phi) \cdot \mathbf{s}} d\mathbf{s} \quad (6)$$

where $\mathbf{k}(\theta, \phi) = k\hat{\mathbf{r}}$ is the wavenumber vector, and $\mathbf{k} \cdot \mathbf{s}$ is the dot product between \mathbf{k} and \mathbf{s} . Denote by $R_r(\theta, \phi)$, $R_\theta(\theta, \phi)$ and $R_\phi(\theta, \phi)$ the components of the radiation vector $\mathbf{R}(\theta, \phi)$ along the $\hat{\mathbf{r}}$, $\hat{\boldsymbol{\theta}}$ and $\hat{\boldsymbol{\phi}}$ directions. Then, we may write:

$$\mathbf{R}(\theta, \phi) = R_r(\theta, \phi)\hat{\mathbf{r}} + R_\theta(\theta, \phi)\hat{\boldsymbol{\theta}} + R_\phi(\theta, \phi)\hat{\boldsymbol{\phi}} \quad (7)$$

where

$$\hat{\mathbf{r}} = \sin \theta \cos \phi \hat{\mathbf{x}} + \sin \theta \sin \phi \hat{\mathbf{y}} + \cos \theta \hat{\mathbf{z}} \quad (8)$$

$$\hat{\boldsymbol{\theta}} = \cos \theta \cos \phi \hat{\mathbf{x}} + \cos \theta \sin \phi \hat{\mathbf{y}} - \sin \theta \hat{\mathbf{z}} \quad (9)$$

$$\hat{\boldsymbol{\phi}} = -\sin \phi \hat{\mathbf{x}} + \cos \phi \hat{\mathbf{y}}. \quad (10)$$

Substituting (7) into (4) yields

$$\mathbf{e}(\mathbf{r}) = G(r) [R_\theta(\theta, \phi)\hat{\boldsymbol{\theta}} + R_\phi(\theta, \phi)\hat{\boldsymbol{\phi}}] \quad (11)$$

since $\hat{\mathbf{r}} \times \hat{\mathbf{r}} = \mathbf{0}$, $(\hat{\mathbf{r}} \times \hat{\boldsymbol{\theta}}) \times \hat{\mathbf{r}} = \hat{\boldsymbol{\theta}}$ and $(\hat{\mathbf{r}} \times \hat{\boldsymbol{\phi}}) \times \hat{\mathbf{r}} = \hat{\boldsymbol{\phi}}$.¹ Notice that $\mathbf{e}(\mathbf{r})$ is completely determined by the transverse component $\mathbf{R}_\perp(\theta, \phi) = R_\theta(\theta, \phi)\hat{\boldsymbol{\theta}} + R_\phi(\theta, \phi)\hat{\boldsymbol{\phi}}$ of the radiation vector $\mathbf{R}(\theta, \phi)$ [25, Ch. 15].

¹Notice that $\hat{\mathbf{r}} \times \hat{\boldsymbol{\theta}} = -\hat{\boldsymbol{\phi}}$, $-\hat{\boldsymbol{\phi}} \times \hat{\mathbf{r}} = \hat{\boldsymbol{\theta}}$, $\hat{\mathbf{r}} \times \hat{\boldsymbol{\phi}} = -\hat{\boldsymbol{\theta}}$ and $-\hat{\boldsymbol{\theta}} \times \hat{\mathbf{r}} = \hat{\boldsymbol{\phi}}$.

Denote by $\xi_x(\mathbf{r})$, $\xi_y(\mathbf{r})$ and $\xi_z(\mathbf{r})$, the cartesian components of $\boldsymbol{\xi}(\mathbf{r})$ along the $\hat{\mathbf{x}}$, $\hat{\mathbf{y}}$ and $\hat{\mathbf{z}}$ directions, respectively. From (3), we have

$$\xi_x(\mathbf{r}) = [\mathbf{e}(\mathbf{r}) + \mathbf{n}(\mathbf{r})] \cdot \hat{\mathbf{x}} = e_x(\mathbf{r}) + n_x(\mathbf{r}) \quad (12)$$

$$\xi_y(\mathbf{r}) = [\mathbf{e}(\mathbf{r}) + \mathbf{n}(\mathbf{r})] \cdot \hat{\mathbf{y}} = e_y(\mathbf{r}) + n_y(\mathbf{r}) \quad (13)$$

$$\xi_z(\mathbf{r}) = [\mathbf{e}(\mathbf{r}) + \mathbf{n}(\mathbf{r})] \cdot \hat{\mathbf{z}} = e_z(\mathbf{r}) + n_z(\mathbf{r}). \quad (14)$$

where $e_x(\mathbf{r})$, $e_y(\mathbf{r})$ and $e_z(\mathbf{r})$ are obtained from (11) by using (8) – (10). This yields

$$e_x(\mathbf{r}) = G(r) [R_\theta(\theta, \phi) \cos \theta \cos \phi - R_\phi(\theta, \phi) \sin \phi] \quad (15)$$

$$e_y(\mathbf{r}) = G(r) [R_\theta(\theta, \phi) \cos \theta \sin \phi + R_\phi(\theta, \phi) \cos \phi] \quad (16)$$

$$e_z(\mathbf{r}) = -G(r) R_\theta(\theta, \phi) \sin \theta. \quad (17)$$

A statistical model for the random field $\mathbf{n}(\mathbf{r})$ is needed. Following [26]–[27], we model $\mathbf{n}(\mathbf{r})$ as a spatially uncorrelated zero-mean complex Gaussian process with correlation function

$$\mathbf{E} \{ \mathbf{n}(\mathbf{r}) \mathbf{n}^\dagger(\mathbf{r}') \} = \sigma^2 \mathbf{I} \delta(\mathbf{r} - \mathbf{r}') \quad (18)$$

where \mathbf{I} is the identity matrix, $\delta(\cdot)$ is the Dirac's delta function, and σ^2 is measured in V^2 , where V indicates volts [27].

B. Problem formulation

We aim at computing the Cramér-Rao bound (CRB) for the estimation of the position of centroid C in Fig. 1 based on the noisy observation vector $\boldsymbol{\xi}(\mathbf{r})$ over the observation region \mathcal{R}_o , whose cartesian components are given by (12) – (14). For this purpose, we call $\mathbf{u} = (x_C, y_C, z_C)$ the unknown vector collecting the coordinates of C with respect to the cartesian system $OXYZ$. The CRB for the estimation of the i th entry of \mathbf{u} , say u_i , is (e.g., [28])

$$\text{CRB}(u_i) = [\mathbf{F}^{-1}]_{ii} \quad (19)$$

where \mathbf{F} is the Fisher's Information Matrix (FIM). The latter is a 3×3 hermitian matrix, whose elements are computed as

$$[\mathbf{F}]_{mn} = \frac{1}{\sigma^2} \int_{-\frac{\ell}{2}}^{\frac{\ell}{2}} \int_{-\frac{\ell}{2}}^{\frac{\ell}{2}} f_{mn}(y, z) dy dz \quad (20)$$

where

$$f_{mn}(y, z) = \frac{\partial e_x(\mathbf{r})}{\partial u_m} \frac{\partial e_x^*(\mathbf{r})}{\partial u_n} + \frac{\partial e_y(\mathbf{r})}{\partial u_m} \frac{\partial e_y^*(\mathbf{r})}{\partial u_n} + \frac{\partial e_z(\mathbf{r})}{\partial u_m} \frac{\partial e_z^*(\mathbf{r})}{\partial u_n} \quad (21)$$

and the integration is performed over the observation region \mathcal{R}_o , as defined in Assumption 1. The functional dependence of $e_x(\mathbf{r})$, $e_y(\mathbf{r})$ and $e_z(\mathbf{r})$ on \mathbf{u} is hidden in the spherical coordinates (r, θ, ϕ) . Indeed, we have

$$r = \|\mathbf{r}\| = \sqrt{x_C^2 + (y - y_C)^2 + (z - z_C)^2} \quad (22)$$

$$\cos \theta = \frac{z - z_C}{r} \quad (23)$$

$$\tan \phi = -\frac{y - y_C}{x_C}. \quad (24)$$

Accordingly, we can write

$$\frac{\partial e_v(\mathbf{r})}{\partial u_i} = \frac{\partial e_v(\mathbf{r})}{\partial r} \frac{\partial r}{\partial u_i} + \frac{\partial e_v(\mathbf{r})}{\partial \theta} \frac{\partial \theta}{\partial u_i} + \frac{\partial e_v(\mathbf{r})}{\partial \phi} \frac{\partial \phi}{\partial u_i} \quad (25)$$

with $v \in \{x, y, z\}$ and $i \in \{1, 2, 3\}$. The derivatives of r , θ and ϕ with respect to u_i can be easily computed from (22) – (24), whereas the partial derivatives of $e_v(\mathbf{r})$ with respect to r , θ and ϕ can be obtained from (15) – (17).

It is clear that the computation of (25) requires knowledge of the components $R_\theta(\theta, \phi)$ and $R_\phi(\theta, \phi)$ of the radiation vector $\mathbf{R}(\theta, \phi)$. In other words, the evaluation of (25) implicitly assumes that current distribution inside the source region \mathcal{R}_s is a priori known. However, this is not always the case in practical applications. When it is *not* a priori known, the problem must be reformulated to take into account this lack of information. In the remainder of this paper, we consider a specific scenario in which the current source is an elementary (i.e., short) dipole with an arbitrary orientation and address the estimation problem in both cases, that is, *with* and *without* a priori knowledge of the current distribution.

C. Discussion

The expression in (11) provides the most general model for the electric field $\mathbf{e}(\mathbf{r})$ in a point \mathbf{r} lying in the Fraunhofer radiation region of the source. Specifically, it takes into account its vector nature as well as dependence on the current distribution inside the transmitting volume. We see that $\mathbf{e}(\mathbf{r})$ is the product of the two terms: $G(r)$ and $\mathbf{R}_\perp(\theta, \phi) = R_\theta(\theta, \phi)\hat{\boldsymbol{\theta}} + R_\phi(\theta, \phi)\hat{\boldsymbol{\phi}}$. The first term is given in (5) and represents a scalar spherical wave, which accounts for the distance r between the source and the point P . In the observation region \mathcal{R}_o , we have that $\mathbf{r} = r_C + \mathbf{d}$, where $r_C = -x_C\hat{\mathbf{x}} + y_C\hat{\mathbf{y}} + z_C\hat{\mathbf{z}}$ is the vector from C to O and $\mathbf{d} = y\hat{\mathbf{y}} + z\hat{\mathbf{z}}$ is the vector from O to P . Accordingly, (22) reduces to

$$r = \|\mathbf{r}_C + \mathbf{d}\| = r_C \sqrt{1 + 2(\hat{\mathbf{r}}_C \cdot \hat{\mathbf{d}}) \frac{d}{r_C} + \frac{d^2}{r_C^2}} \quad (26)$$

with $r_C = \|\mathbf{r}_C\|$ and $d = \|\mathbf{d}\|$. In the case $r_C \gg d$, we can replace r with r_C in the denominator of (5) and obtain the following approximation:

$$G(r) \approx -jkZ_0 \frac{e^{-jkr}}{4\pi r_C}. \quad (27)$$

As for the exponent e^{-jkr} , a better approximation may be obtained by considering the Taylor series expansion $\sqrt{1+x} \approx 1 + x/2 - x^2/8$, valid for small values of x . Applying this approximation to (26) yields

$$r \approx r_C + (\hat{\mathbf{r}}_C \cdot \hat{\mathbf{d}})d + [1 - (\hat{\mathbf{r}}_C \cdot \hat{\mathbf{d}})^2]d^2/2r_C \quad (28)$$

and (27) thus reduces to

$$G(r) \approx -jkZ_0 \frac{e^{-jkr_C}}{4\pi r_C} e^{-jk[d \cos \psi + \sin^2 \psi (d^2/2r_C)]} \quad (29)$$

where we have called $\cos \psi = (\hat{\mathbf{r}}_C \cdot \hat{\mathbf{d}})$. This expansion is called the *Fresnel approximation* [11]. In the case $r_C \gg L^2/\lambda$, we can retain only the first-order term in the exponent of (29) and thus obtain

$$G(r) \approx -jkZ_0 \frac{e^{-jkr_C}}{4\pi r_C} e^{-jkd \cos \psi} \quad (30)$$

which represents the well-known planar approximation of the spherical wave in (5).

Consider now the term $\mathbf{R}_\perp(\theta, \phi) = R_\theta(\theta, \phi)\hat{\boldsymbol{\theta}} + R_\phi(\theta, \phi)\hat{\boldsymbol{\phi}}$ in (11), which depends only on the components along $\hat{\boldsymbol{\theta}}$ and $\hat{\boldsymbol{\phi}}$ of the radiation vector $\mathbf{R}(\theta, \phi)$ in (6). Notice that the exponential factor $e^{jk(\theta, \phi) \cdot \mathbf{s}}$ in (6) can be ignored, provided that $l_s \ll \lambda$. For example, this happens with a *point source* (also known as Hertzian dipole [24, Sec. 2.3.1]) that has been largely studied in the literature, and will also be considered in the remainder of this paper. In such a case, (6) reduces to

$$\mathbf{R}(\theta, \phi) = \int_{\mathcal{R}_s} \mathbf{j}(\mathbf{s}) d\mathbf{s} \quad (31)$$

so that

$$\begin{aligned} R_\theta(\theta, \phi) &= \int_{\mathcal{R}_s} j_\theta(\mathbf{s}) d\mathbf{s} \\ &= J_x \cos \theta \cos \phi + J_y \cos \theta \sin \phi - J_z \sin \theta \end{aligned} \quad (32)$$

and

$$R_\phi(\theta, \phi) = \int_{\mathcal{R}_s} j_\phi(\mathbf{s}) d\mathbf{s} = -J_x \sin \phi + J_y \cos \phi \quad (33)$$

with $J_\nu = \int_{\mathcal{R}_s} j_\nu(\mathbf{s}) d\mathbf{s}$. The above expressions show that, in general, the dependence of $R_\theta(\theta, \phi)$ and $R_\phi(\theta, \phi)$ on θ and ϕ cannot be ignored, even assuming a point source. On the other hand, when the solid angle subtended by the square domain \mathcal{R}_o is small, which amounts to saying that the ratio between the observation area and the squared distance is small (i.e., $L^2/r_C^2 \approx 0$), then the following approximations can be made at each point of \mathcal{R}_o ,

$$\theta \approx \theta_o \quad \phi \approx \phi_o \quad (34)$$

where $\theta_o = \arccos(-z_C/r_C)$ and $\phi_o = \arctan y_C/x_C$ are the polar and azimuthal angles of O , respectively. In such a case, $R_\theta(\theta, \phi)$ and $R_\phi(\theta, \phi)$ become (approximately) independent of θ and ϕ , and are given by

$$R_\theta(\theta, \phi) = J_x \cos \theta_o \cos \phi_o + J_y \cos \theta_o \sin \phi_o - J_z \sin \theta_o$$

$$R_\phi(\theta, \phi) = -J_x \sin \phi_o + J_y \cos \phi_o$$

For example, assume that the source is on the line perpendicular to \mathcal{R}_o passing through O , which means that $\theta_o = \pi/2$ and $\phi_o = \pi$, and that $J_x = J_y = 0$ (i.e., $\mathbf{j}(\mathbf{s})$ is vertically directed). In such a case, $R_\theta(\theta, \phi) = -J_z \sin \theta$ and $R_\phi(\theta, \phi) = 0$. For a point $P \in \mathcal{R}_o$, we have $\theta \in [\theta_o - \arctan(L/2r_C), \theta_o + \arctan(L/2r_C)]$, which show that the approximation $\theta \approx \theta_o$ becomes more and more accurate as L/r_C decreases, as expected. For $L = 3$ m and $r_C = 10$ m we have $\arctan(L/2r_C) \approx 5 \times 10^{-2}\pi$ and $\sin \theta \in (0.989, 1]$.

Remark 1. A different approach for estimating the position of C is to make use of a scalar, instead of a vector, field. For example, one could use only one of the three components of $\mathbf{e}(\mathbf{r})$. This may simplify the analysis but would result in lower performance, i.e., a larger CRB. An alternative approach is to consider a scalar field that is related to the component of the Poynting vector perpendicular in each point to the planar

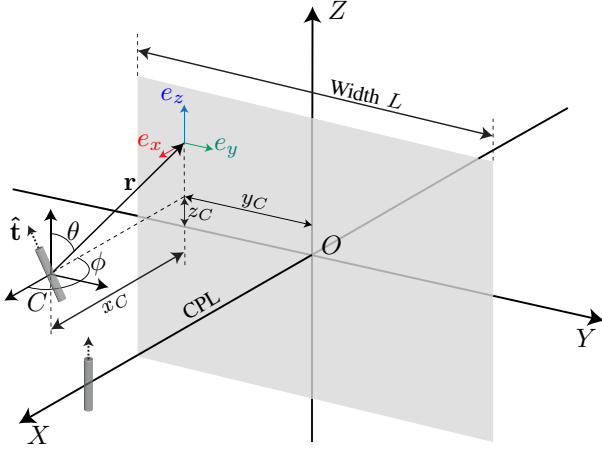


Fig. 2: Source model and CPL assumption.

region. This component is proportional to $\|\mathbf{e}(\mathbf{r})\|^2 \sin \theta \cos \phi$, and the associated scalar field is

$$\begin{aligned} E &\triangleq e^{-jkr} \sqrt{\|\mathbf{e}(\mathbf{r})\|^2 \sin \theta \cos \phi} \\ &= kZ_0 \frac{e^{-jkr} \sqrt{x_C}}{4\pi r^{3/2}} \sqrt{R_\theta^2(\theta, \phi) + R_\phi^2(\theta, \phi)}. \end{aligned} \quad (35)$$

In the case of an isotropic radiating source, $R_\theta^2(\theta, \phi) + R_\phi^2(\theta, \phi)$ is independent of θ and ϕ , and thus (35) reduces to the scalar model considered in [7, Eq. (2)]. We stress that this scalar model represents a specific case, which is not valid in general. We will use (35) in the numerical analysis for comparisons.

III. CRB COMPUTATION WITH AN ELEMENTARY SOURCE DIPOLE

To simplify the analysis, we make the following assumption about the source, as shown in Fig. 2.

Assumption 3. The source is an elementary dipole of length l_s pointing in an arbitrary direction $\hat{\mathbf{t}} = t_x \hat{\mathbf{x}} + t_y \hat{\mathbf{y}} + t_z \hat{\mathbf{z}}$ or, equivalently, $\hat{\mathbf{t}} = t_r(\theta, \phi) \hat{\mathbf{r}} + t_\theta(\theta, \phi) \hat{\boldsymbol{\theta}} + t_\phi(\theta, \phi) \hat{\boldsymbol{\phi}}$, with

$$t_r(\theta, \phi) = \sin \theta \cos \phi t_x + \sin \theta \sin \phi t_y + \cos \theta t_z \quad (36)$$

$$t_\theta(\theta, \phi) = \cos \theta \cos \phi t_x + \cos \theta \sin \phi t_y - \sin \theta t_z \quad (37)$$

$$t_\phi(\theta, \phi) = -\sin \phi t_x + \cos \phi t_y. \quad (38)$$

In the case of an elementary dipole, the current density $\mathbf{j}(\mathbf{s})$ has the following expression (e.g. [24, Sec. 2.3.1])

$$\mathbf{j}(\mathbf{s}) = I_{in} l_s \delta(\mathbf{s}) \hat{\mathbf{t}} \quad (39)$$

where I_{in} is the uniform current level in the dipole. Plugging (39) into (6) yields

$$\mathbf{R}(\theta, \phi) = I_{in} l_s \hat{\mathbf{t}}. \quad (40)$$

By using the representation of $\hat{\mathbf{t}}$ in terms of $(\hat{\mathbf{r}}, \hat{\boldsymbol{\theta}}, \hat{\boldsymbol{\phi}})$, from (7) we have that

$$R_\theta(\theta, \phi) = I_{in} l_s t_\theta(\theta, \phi) \quad (41)$$

$$R_\phi(\theta, \phi) = I_{in} l_s t_\phi(\theta, \phi) \quad (42)$$

from which it follows that the electric vector field $\mathbf{e}(\mathbf{r})$ in (11) takes the following form:

$$\mathbf{e}(\mathbf{r}) = G(r) I_{in} l_s [t_\theta(\theta, \phi) \hat{\boldsymbol{\theta}} + t_\phi(\theta, \phi) \hat{\boldsymbol{\phi}}]. \quad (43)$$

An equivalent expression of $\mathbf{e}(\mathbf{r})$ in terms of the cartesian components (t_x, t_y, t_z) of $\hat{\mathbf{t}}$ can be obtained by substituting (40) into (4) to obtain

$$\mathbf{e}(\mathbf{r}) = G(r) I_{in} l_s [\hat{\mathbf{t}} - (\hat{\mathbf{r}} \cdot \hat{\mathbf{t}}) \hat{\mathbf{r}}] \quad (44)$$

where we have used the identity $(\hat{\mathbf{r}} \times \hat{\mathbf{t}}) \times \hat{\mathbf{r}} = \hat{\mathbf{t}} - (\hat{\mathbf{r}} \cdot \hat{\mathbf{t}}) \hat{\mathbf{r}}$. From (5) and (44), it thus follows that

$$e_x = -j\chi \frac{e^{-jkr}}{r} [t_x - (r_x t_x + r_y t_y + r_z t_z) r_x] \quad (45)$$

$$e_y = -j\chi \frac{e^{-jkr}}{r} [t_y - (r_x t_x + r_y t_y + r_z t_z) r_y] \quad (46)$$

$$e_z = -j\chi \frac{e^{-jkr}}{r} [t_z - (r_x t_x + r_y t_y + r_z t_z) r_z]. \quad (47)$$

where (r_x, r_y, r_z) are the cartesian components of $\hat{\mathbf{r}}$, and

$$\chi = \frac{Z_0 I_{in} l_s}{2 \lambda} \quad (48)$$

is measured in volts, V. For the sake of simplicity, we have dropped the dependence of e_x , e_y and e_z on \mathbf{r} . The above expressions depend on (t_x, t_y, t_z) and the cartesian coordinates (x_C, y_C, z_C) of the centroid C , which are related to (r_x, r_y, r_z) through the following equations:

$$r_x = -\frac{x_C}{r}, \quad r_y = \frac{y - y_C}{r}, \quad r_z = \frac{z - z_C}{r} \quad (49)$$

where r is given by (22).

We aim at evaluating the CRBs for the estimation of (x_C, y_C, z_C) on the basis of (45)–(47). We first consider the case in which the parameters (t_x, t_y, t_z) are *unknown* and thus must be considered as *nuisance* parameters. This corresponds to the case of having *partial* information about the source current distribution. This first case is not only more general but also instrumental to obtain the CRBs with *full* information, i.e., the parameters (t_x, t_y, t_z) are a priori *known*.

A. Unknown orientation of the dipole

When (t_x, t_y, t_z) are unknown, we cannot use (19)–(21) but must compute the FIM for *all* the unknown parameters, which are collected into the 6-dimensional vector $\mathbf{p} = (t_x, t_y, t_z, x_C, y_C, z_C)$. Therefore, the FIM is a 6×6 hermitian matrix with entries given by

$$[\mathbf{F}]_{mn} = \frac{1}{\sigma^2} \int_{-\frac{L}{2}}^{\frac{L}{2}} \int_{-\frac{L}{2}}^{\frac{L}{2}} \left[\frac{\partial e_x}{\partial p_m} \frac{\partial e_x^*}{\partial p_n} + \frac{\partial e_y}{\partial p_m} \frac{\partial e_y^*}{\partial p_n} + \frac{\partial e_z}{\partial p_m} \frac{\partial e_z^*}{\partial p_n} \right] dy dz \quad (50)$$

where p_m denotes the m th element of \mathbf{p} . The derivatives involved in $[\mathbf{F}]_{mn}$ are computed in Appendix A. The matrix \mathbf{F} can be partitioned as [28]

$$\mathbf{F} = \begin{bmatrix} \mathbf{F}_{tt} & \mathbf{F}_{tc} \\ \mathbf{F}_{ct} & \mathbf{F}_{cc} \end{bmatrix} \quad (51)$$

where the 3×3 blocks \mathbf{F}_{tt} and \mathbf{F}_{cc} contain the partial derivatives with respect to (t_x, t_y, t_z) and (x_C, y_C, z_C) , respectively, while \mathbf{F}_{tc} and \mathbf{F}_{ct} contain the mixed derivatives. Since \mathbf{F} is hermitian, we have $\mathbf{F}_{tt} = \mathbf{F}_{tt}^H$, $\mathbf{F}_{cc} = \mathbf{F}_{cc}^H$ and $\mathbf{F}_{tc} = \mathbf{F}_{ct}^H$. Based on (51) and well known formulas, we can immediately show that the CRBs for the estimation of x_C , y_C and z_C , are given by the diagonal elements of the matrix $(\mathbf{F}_{cc} - \mathbf{F}_{tc}^H \mathbf{F}_{tt}^{-1} \mathbf{F}_{tc})^{-1}$, i.e.,

$$\text{CRB}_u(x_C) = \left[(\mathbf{F}_{cc} - \mathbf{F}_{tc}^H \mathbf{F}_{tt}^{-1} \mathbf{F}_{tc})^{-1} \right]_{11} \quad (52)$$

$$\text{CRB}_u(y_C) = \left[(\mathbf{F}_{cc} - \mathbf{F}_{tc}^H \mathbf{F}_{tt}^{-1} \mathbf{F}_{tc})^{-1} \right]_{22} \quad (53)$$

$$\text{CRB}_u(z_C) = \left[(\mathbf{F}_{cc} - \mathbf{F}_{tc}^H \mathbf{F}_{tt}^{-1} \mathbf{F}_{tc})^{-1} \right]_{33} \quad (54)$$

where the subscript $_u$ is used to stress that the above results refer to the case of *unknown* dipole orientation.

B. Known orientation of dipole

When the arbitrary parameters (t_x, t_y, t_z) of the dipole are perfectly known, we have a complete description of the source current distribution. This means that the functions $R_\theta(\theta, \phi)$ and $R_\phi(\theta, \phi)$ are known, and we can compute the CRB following the general² procedure outlined in Section II-B. The Fisher's information matrix obtained in this way coincides with the matrix \mathbf{F}_{cc} computed previously. It thus follows that the CRBs for the estimation of x_C , y_C and z_C , can be found as the diagonal elements of the matrix \mathbf{F}_{cc}^{-1} , i.e.,

$$\text{CRB}(x_C) = [\mathbf{F}_{cc}^{-1}]_{11} \quad (55)$$

$$\text{CRB}(y_C) = [\mathbf{F}_{cc}^{-1}]_{22} \quad (56)$$

$$\text{CRB}(z_C) = [\mathbf{F}_{cc}^{-1}]_{33}. \quad (57)$$

By applying the matrix inversion lemma,³ we obtain

$$\begin{aligned} & \left[(\mathbf{F}_{cc} - \mathbf{F}_{tc}^H \mathbf{F}_{tt}^{-1} \mathbf{F}_{tc})^{-1} \right]_{ii} \\ &= [\mathbf{F}_{cc}^{-1}]_{ii} + \left[\mathbf{F}_{cc}^{-1} \mathbf{F}_{tc}^H (\mathbf{F}_{tt} - \mathbf{F}_{tc} \mathbf{F}_{cc}^{-1} \mathbf{F}_{tc}^H)^{-1} \mathbf{F}_{tc} \mathbf{F}_{cc}^{-1} \right]_{ii} \end{aligned} \quad (58)$$

for $i = 1, 2, 3$. Notice that $(\mathbf{F}_{tt} - \mathbf{F}_{tc} \mathbf{F}_{cc}^{-1} \mathbf{F}_{tc}^H)^{-1}$ is positive semi-definite, since it is the 3×3 block in the upper left corner of the semi-positive definite matrix \mathbf{F}^{-1} . As a result, the second matrix $\mathbf{F}_{cc}^{-1} \mathbf{F}_{tc}^H (\mathbf{F}_{tt} - \mathbf{F}_{tc} \mathbf{F}_{cc}^{-1} \mathbf{F}_{tc}^H)^{-1} \mathbf{F}_{tc} \mathbf{F}_{cc}^{-1}$ in (58) is positive semi-definite as well. Hence, from (58) it follows that

$$[\mathbf{F}_{cc}^{-1}]_{ii} \leq \left[(\mathbf{F}_{cc} - \mathbf{F}_{tc}^H \mathbf{F}_{tt}^{-1} \mathbf{F}_{tc})^{-1} \right]_{ii}. \quad (59)$$

By exploiting this result, we have that

$$\text{CRB}(x_C) \leq \text{CRB}_u(x_C) \quad (60)$$

$$\text{CRB}(y_C) \leq \text{CRB}_u(y_C) \quad (61)$$

$$\text{CRB}(z_C) \leq \text{CRB}_u(z_C) \quad (62)$$

as it should be since the Cramér-Rao bound worsens in the presence of unknown nuisance parameters.

²Here, by *general* we mean that it is valid irrespective of the particular current distribution, as long as the latter is known.

³ $(\mathbf{A} + \mathbf{UCV})^{-1} = \mathbf{A}^{-1} - \mathbf{A}^{-1} \mathbf{U}(\mathbf{C}^{-1} + \mathbf{V} \mathbf{A}^{-1} \mathbf{U})^{-1} \mathbf{V} \mathbf{A}^{-1}$

IV. A CASE STUDY

The elements of the matrices needed for the computation of \mathbf{F} in (51) can be obtained by numerically evaluating the integrals (50) for any arbitrary position of the dipole. Although possible, this makes it hard to gain insights into the CRBs. Next, we show that closed-form expressions can be obtained when the dipole is located in the central perpendicular line (CPL) and is vertically oriented; see Fig. 2. The following assumption is thus made.

Assumption 4. *The center C of the dipole is on the line perpendicular to \mathcal{R}_o passing through the point O (known as CPL case), as shown in Fig. 2, and the dipole is vertically oriented.*

Under the CPL assumption, we have that $y_C = z_C = 0$, whereas the vertical orientation of the dipole implies that $t_x = t_y = 0$ and $t_z = 1$. For convenience, we call

$$\text{SNR} \triangleq \frac{|\chi|^2}{\sigma^2} \quad (63)$$

the signal-to-noise ratio (SNR) with χ given by (48) and define

$$\rho \triangleq \frac{L}{x_C}. \quad (64)$$

The following result is obtained.

Proposition 1. *Under Assumption 4, we have that:*

- 1) *The matrix \mathbf{F}_{cc} becomes diagonal with entries*

$$[\mathbf{F}_{cc}]_{11} = \text{SNR} \cdot [k^2 \mathcal{J}_1(\rho) + x_C^{-2} \mathcal{J}_2(\rho)] \quad (65)$$

$$[\mathbf{F}_{cc}]_{22} = \text{SNR} \cdot [k^2 \mathcal{J}_3(\rho) + x_C^{-2} \mathcal{J}_4(\rho)] \quad (66)$$

$$[\mathbf{F}_{cc}]_{33} = \text{SNR} \cdot [k^2 \mathcal{J}_5(\rho) + x_C^{-2} \mathcal{J}_6(\rho)] \quad (67)$$

where $\mathcal{J}_i(\rho)$ for $i = 1, \dots, 6$ are given in Appendix B.

- 2) *The matrix \mathbf{F}_{tt} becomes diagonal with entries*

$$[\mathbf{F}_{tt}]_{11} = \text{SNR} \cdot \mathcal{J}_7(\rho) \quad (68)$$

$$[\mathbf{F}_{tt}]_{22} = [\mathbf{F}_{tt}]_{33} = \text{SNR} \cdot \mathcal{J}_8(\rho) \quad (69)$$

where $\mathcal{J}_i(\rho)$ for $i = 7, 8$ are given in (100)–(101) in Appendix B.

- 3) *The elements of \mathbf{F}_{tc} are all zero except for $[\mathbf{F}_{tc}]_{13}$ and $[\mathbf{F}_{tc}]_{31}$ which can be computed as*

$$[\mathbf{F}_{tc}]_{13} = k \text{SNR} \cdot \mathcal{J}_9(\rho) \quad (70)$$

$$[\mathbf{F}_{tc}]_{31} = \text{SNR} \cdot [k \mathcal{J}_{10}(\rho) + x_C^{-1} \mathcal{J}_{11}(\rho)] \quad (71)$$

where $\mathcal{J}_i(\rho)$ for $i = 9, 10, 11$ are given in (104)–(106) in Appendix B.

Proof. The proof is given in Appendix B.

Based on the results in Proposition 1, the following corollaries are obtained for both cases with unknown and known dipole orientation. Notice that the dependence on ρ is omitted to simplify the notation.

Corollary 1 (Unknown dipole orientation). *Under Assumption 4, the CRBs for the estimation of x_C , y_C and z_C when the dipole orientation is unknown are given by*

$$\text{CRB}_u(x_C) = \frac{\text{SNR}^{-1}}{k^2 \mathcal{J}_1 + x_C^{-2} \mathcal{J}_2 - \mathcal{J}_8^{-1} |k \mathcal{J}_{10} + x_C^{-1} \mathcal{J}_{11}|^2} \quad (72)$$

$$\text{CRB}_u(y_C) = \frac{\text{SNR}^{-1}}{k^2 \mathcal{J}_3 + x_C^{-2} \mathcal{J}_4} \quad (73)$$

$$\text{CRB}_u(z_C) = \frac{\text{SNR}^{-1}}{k^2 (\mathcal{J}_5 - \mathcal{J}_7^{-1} |\mathcal{J}_9|^2) + x_C^{-2} \mathcal{J}_6}. \quad (74)$$

Proof. The proof follows from (52) – (54) by using the results of Proposition 1 from which it follows that $\mathbf{F}_{tc}^H \mathbf{F}_{tt}^{-1} \mathbf{F}_{tc} = \text{diag}(|[\mathbf{F}_{tc}]_{31}|^2 / [\mathbf{F}_{tt}]_{33}, 0, |[\mathbf{F}_{tc}]_{13}|^2 / [\mathbf{F}_{tt}]_{11})$.

Corollary 2 (Known dipole orientation). *Under Assumption 4, the CRBs for the estimation of x_C , y_C and z_C when the dipole orientation is known are:*

$$\text{CRB}(x_C) = \frac{\text{SNR}^{-1}}{k^2 \mathcal{J}_1 + x_C^{-2} \mathcal{J}_2} \quad (75)$$

$$\text{CRB}(y_C) = \frac{\text{SNR}^{-1}}{k^2 \mathcal{J}_3 + x_C^{-2} \mathcal{J}_4} \quad (76)$$

$$\text{CRB}(z_C) = \frac{\text{SNR}^{-1}}{k^2 \mathcal{J}_5 + x_C^{-2} \mathcal{J}_6}. \quad (77)$$

Proof. It easily follows from Proposition 1 by using (55)–(57).

The above corollaries clearly show the effects of the wavelength $\lambda = 2\pi/k$ and x_C for fixed values of ρ or, equivalently, of the functions $\{\mathcal{J}_i\}$. Particularly, we see that the estimation accuracy increases as λ or x_C decrease for fixed values of SNR. Similar results were already observed in [7].

A. Analysis for $x_C \gg \lambda$

Assumption 4 leads to a considerable simplification since the matrices \mathbf{F}_{cc} and $\mathbf{F}_{tc}^H \mathbf{F}_{tt}^{-1} \mathbf{F}_{tc}$ become diagonal. Further simplifications can be obtained when $x_C \gg \lambda$. This condition is always satisfied in systems operating at frequencies in the range of GHz or above.

Proposition 2. *Under Assumption 4 and $x_C \gg \lambda$, then CRBs for the case in which the dipole orientation is unknown reduce to*

$$\text{CRB}_u(x_C) \approx \frac{\text{SNR}^{-1}}{\mathcal{J}_1 - \mathcal{J}_8^{-1} |\mathcal{J}_{10}|^2} \cdot \frac{\lambda^2}{4\pi^2} \quad (78)$$

$$\text{CRB}_u(y_C) \approx \frac{\text{SNR}^{-1}}{\mathcal{J}_3} \cdot \frac{\lambda^2}{4\pi^2} \quad (79)$$

while those for the case in which the dipole orientation is known become

$$\text{CRB}(x_C) \approx \frac{\text{SNR}^{-1}}{\mathcal{J}_1} \cdot \frac{\lambda^2}{4\pi^2} \quad (80)$$

$$\text{CRB}(y_C) = \text{CRB}_u(y_C). \quad (81)$$

Proof. See Appendix C.

Proposition 2 shows that, when $x_C \gg \lambda$, the accuracy in the estimation of x_C and y_C solely depends on the values of λ and ρ . In particular, keeping ρ fixed, the CRBs for x_C and y_C scale with the square of λ . On the other hand, for a given value of λ , if x_C increases by a factor α , we must scale L by the same factor in order to keep ρ , and hence the estimation accuracy, unchanged. This means that the area of the observation region must be increased by a factor α^2 . The same conclusions do not hold for the estimation of z_C . Indeed, under Assumption 4 and $x_C \gg \lambda$ it can be shown that the term $x_C^{-2} \mathcal{J}_6$ is not negligible with respect to the other ones appearing in the denominator of the expressions for $\text{CRB}_u(z_C)$ and $\text{CRB}(z_C)$ in Corollaries 1 and 2. Hence, the CRBs cannot be simplified and continue to depend on both x_C and λ .

B. Asymptotic Analysis for $\rho \rightarrow \infty$

Starting from the results given above, it is interesting to analyze the behaviour of the CRBs in the asymptotic regime $\rho = L/x_C \rightarrow \infty$. The main results are summarized in the following proposition.

Proposition 3. *Under Assumption 4 and $x_C \gg \lambda$, in the asymptotic regime $\rho \rightarrow \infty$ we have*

$$\lim_{\rho \rightarrow \infty} \text{CRB}_u(x_C) = \lim_{\rho \rightarrow \infty} \text{CRB}(x_C) = \frac{\text{SNR}^{-1}}{3\pi^3} \lambda^2 \quad (82)$$

$$\lim_{\rho \rightarrow \infty} \text{CRB}_u(y_C) = \lim_{\rho \rightarrow \infty} \text{CRB}(y_C) = \frac{\text{SNR}^{-1}}{3\pi^3} \frac{\lambda^2}{\ln \rho} \quad (83)$$

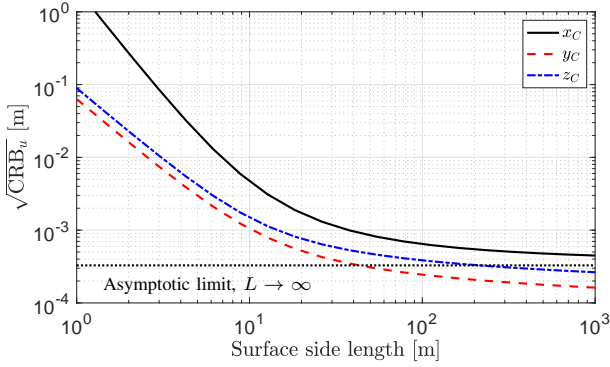
$$\lim_{\rho \rightarrow \infty} \text{CRB}_u(z_C) = \lim_{\rho \rightarrow \infty} \text{CRB}(z_C) = \frac{\text{SNR}^{-1}}{\pi^3} \frac{\lambda^2}{\ln \rho}. \quad (84)$$

Proof. See Appendix D.

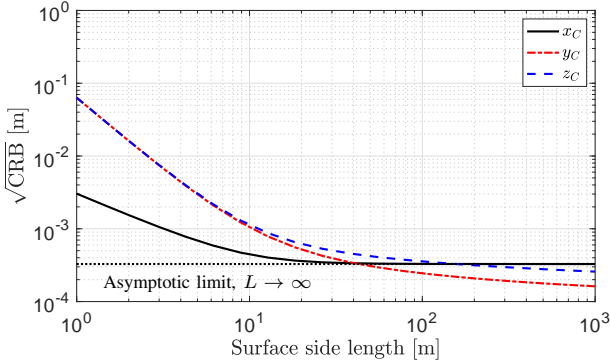
Proposition 3 shows that, for sufficiently large values of $\rho = L/x_C$, the estimation accuracy is the same in both cases of unknown or known dipole orientation. This means that, even though $\hat{\mathbf{t}}$ is unknown, we can achieve the same accuracy in the estimation of the source position as in the case of known dipole orientation. Clearly, this requires in general the *joint* estimation of $\hat{\mathbf{t}}$ and (x_C, y_C, z_C) . It is interesting to note that the CRBs for the estimation of y_C and z_C goes to zero as ρ increases unboundedly. This is in contrast to the results in [7, Eq. (26)] where it is shown that the asymptotic CRBs are identical for all the three dimensions and depend solely on the wavelength λ . This difference is a direct consequence of the different radiation and signal models used for the computation of CRBs. Indeed, in [7] the source is assumed to radiate isotropically and the scalar field (35) is used for deriving the bounds.

V. NUMERICAL ANALYSIS

The effect of the various system parameters on the estimation accuracy are now analyzed by numerically evaluating the CRBs according to the general expressions given in (52)–(54) or in (55)–(57) for the unknown or known dipole orientation cases, respectively. We assume that the dipole is located at a distance $x_C = 6$ m, the signal-to-noise ratio is $\text{SNR} = |\chi|^2 / \sigma^2 = 0$ dB, and the wavelength is $\lambda = 0.01$ m (corresponding to $f_c = 30$ GHz), unless otherwise specified.



(a) Unknown dipole orientation



(b) Known dipole orientation

Fig. 3: RCRBs as a function of the surface side length for a vertically oriented dipole in CPL at a distance $x_C = 6$ m.

Fig. 3 shows the square root of the CRBs (RCRB), measured in meters [m], for the three components x_C , y_C and z_C , as a function of the surface side length L , for a vertically oriented dipole located in CPL, i.e., under the hypotheses of Assumption 4. Both cases of unknown and known orientation are considered in Fig. 3a and Fig. 3b, respectively. We see that all the RCRBs decrease fast with the surface side length, at least for values of L of practical interest, i.e. in the range $1 \text{ m} \leq L \leq 10 \text{ m}$. When the dipole orientation is unknown, $\text{RCRB}(x_C)$ is greater than $\text{RCRB}(y_C)$ and $\text{RCRB}(z_C)$ for all values of L , and approaches the square root of the asymptotic limit (82) for $L > 10^3$ m. On the other hand, when $\hat{\mathbf{t}}$ is known $\text{RCRB}(x_C)$ is much lower than $\text{RCRB}(y_C)$ and $\text{RCRB}(z_C)$ in the range $1 \text{ m} \leq L \leq 10 \text{ m}$, and the asymptotic limit is reached in practice already from $L \approx 20$ m. In both cases, $\text{RCRB}(y_C)$ and $\text{RCRB}(z_C)$ decrease unboundedly as predicted by (83) and (84). It is worthwhile to note that an accuracy on the order of tens of centimeters in all the three dimensions (as required for example in future automotive and industrial applications, e.g., [29]) is achieved for $L \approx 3$ m, both with known or unknown orientation.

To quantify the impact of dipole orientation, Fig. 4a and Fig. 4b show the RCRBs for two different values of $\hat{\mathbf{t}}$, namely $\hat{\mathbf{t}} = (1, 0, 0)$ and $\hat{\mathbf{t}} = (1/\sqrt{3}, 1/\sqrt{3}, 1/\sqrt{3})$. In both cases, the dipole is in CPL and its orientation is unknown. Compared to Fig. 3a, a sensible loss is evident only when $\hat{\mathbf{t}} = (1, 0, 0)$ and for small values of L . For example, with $L = 3$ m the accuracy

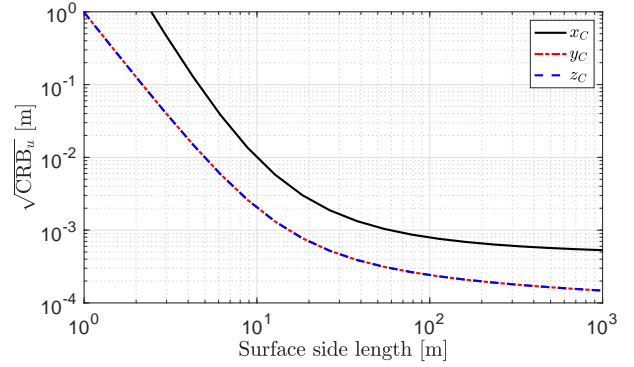
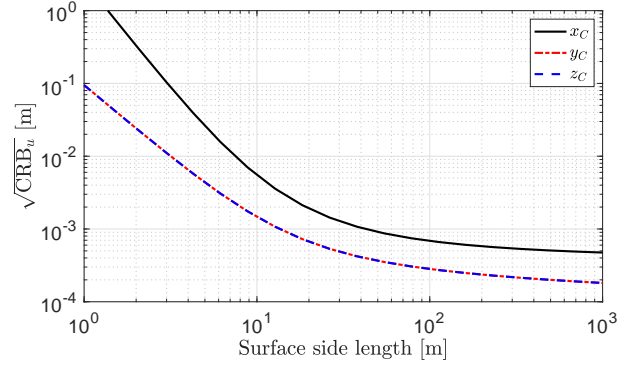
(a) Unknown dipole orientation, $\hat{\mathbf{t}} = (1, 0, 0)$ (b) Unknown dipole orientation, $\hat{\mathbf{t}} = (1, 1, 1)/\sqrt{3}$

Fig. 4: RCRBs as a function of the surface side length for two different (unknown) dipole orientations.

in the estimation of x_C decreases from 10 cm to 1 m. Notice that, for both $\hat{\mathbf{t}} = (1, 0, 0)$ and $\hat{\mathbf{t}} = (1/\sqrt{3}, 1/\sqrt{3}, 1/\sqrt{3})$, the accuracy in the estimation of y_C and z_C is the same. Similar conclusions hold when the dipole orientation is known.

Figs. 5 and 6 show the RCRBs in the case of unknown and known orientation, respectively, as a function of y_C and z_C when $x_C = 6$ m. The dipole is oriented vertically and $L = 3$ m. The value of the RCRB corresponding to a point (y_C, z_C) is measured by the color of that point. More precisely, the RCRB values are first normalized to their minimum, which is achieved when the dipole is in CPL ($y_C = z_C = 0$), and then the normalized values (in dB) are mapped into a colour: higher values are associated to warm colours, lower values to cool ones. This means, for example, that the blue zones in each figure correspond to the best estimation accuracy. Figs. 5 and 6 clearly show the different behaviours of the various RCRBs when the dipole moves away from the CPL position. For example, if we consider Figs. 5a–5c, corresponding to an unknown dipole orientation, we see that $\sqrt{\text{CRB}_u}(y_C)$ decreases faster than $\sqrt{\text{CRB}_u}(x_C)$ and $\sqrt{\text{CRB}_u}(z_C)$ when the dipole moves along the y -direction. On the other hand, when the dipole moves along the z -axis $\sqrt{\text{CRB}_u}(z_C)$ decreases faster than the other RCRBs. The situation is different when the dipole orientation is known. In this case, Figs. 6a–6c show $\sqrt{\text{CRB}_u}(x_C)$ decreases faster than the others whatever the direction of motion is.

Fig. 7 shows the RCRBs as a function of x_C for two

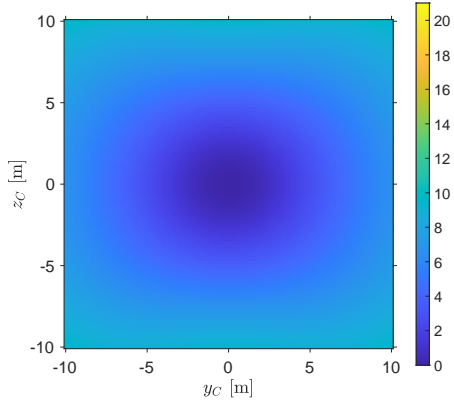
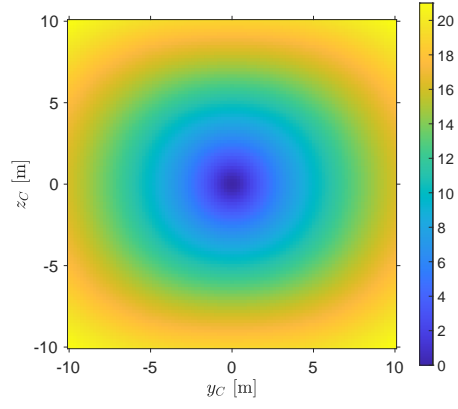
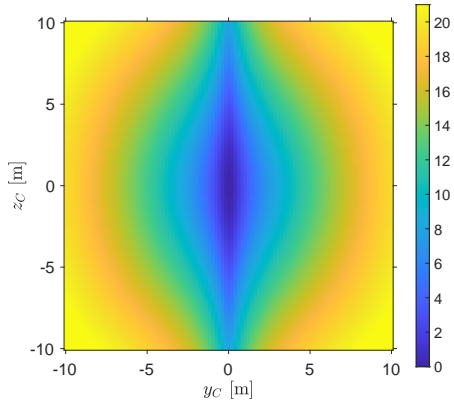
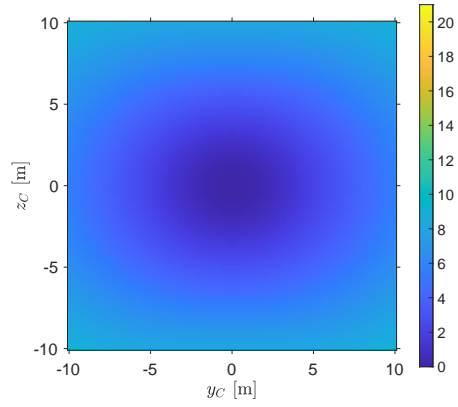
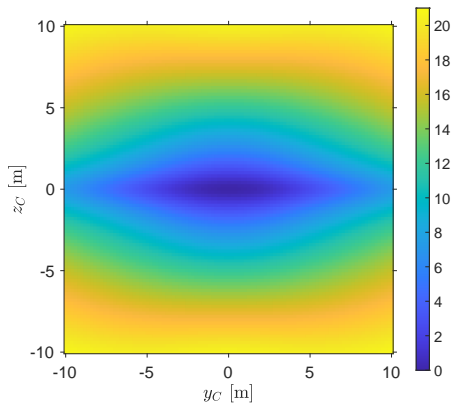
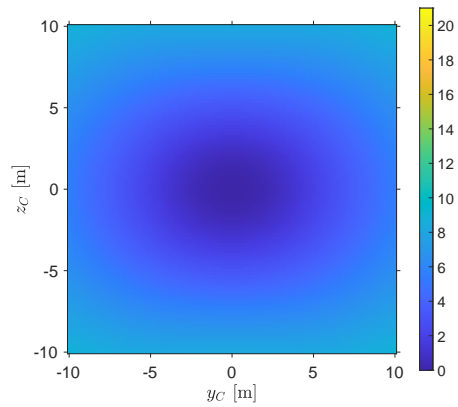
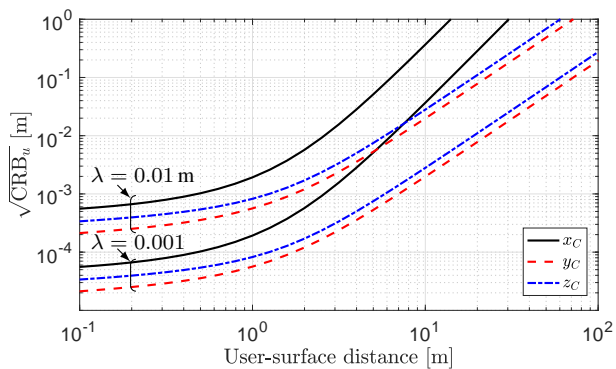
(a) $\sqrt{\text{CRB}_u(x_C)}$ as a function of y_C and z_C (a) $\sqrt{\text{CRB}(x_C)}$ as a function of y_C and z_C (b) $\sqrt{\text{CRB}_u(y_C)}$ as a function of y_C and z_C (b) $\sqrt{\text{CRB}(y_C)}$ as a function of y_C and z_C (c) $\sqrt{\text{CRB}_u(z_C)}$ as a function of y_C and z_C (c) $\sqrt{\text{CRB}(z_C)}$ as a function of y_C and z_C

Fig. 5: RCRBs in the case of unknown orientation as a function of y_C and z_C when $x_C = 6$ m. The dipole is oriented vertically and $L = 3$ m.

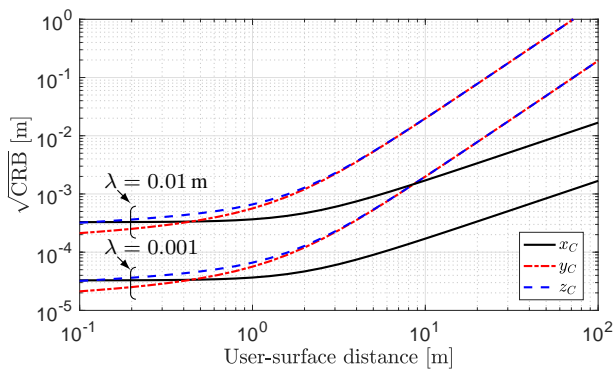
Fig. 6: RCRBs in the case of known orientation as a function of y_C and z_C when $x_C = 6$ m. The dipole is oriented vertically and $L = 3$ m.

different values of the wavelength, namely $\lambda = 0.01$ m (corresponding to $f_c = 30$ GHz) and $\lambda = 0.001$ m (corresponding to $f_c = 300$ GHz). The dipole is in CPL and is oriented

vertically. The surface side length is $L = 3$ m. As expected, the estimation accuracy reduces as the distance between the source and the observation region increases. In particular, it



(a) Unknown dipole orientation



(b) Known dipole orientation

Fig. 7: RCRBs as a function of x_C for a vertical dipole in CPL and $L = 3$ m, with $\lambda = 0.01$ or 0.001 m.

can be seen that, in the absence of information about the dipole orientation, $\text{RCRB}(x_C)$ increases faster than $\text{RCRB}(y_C)$ and $\text{RCRB}(z_C)$, whereas the exact opposite is observed in the case of a known orientation. It is worth noting that, in both cases, the RCRBs depend linearly on λ , at least in the range of values of x_C (and hence ρ) considered. Indeed, reducing the wavelength of a factor ten reduces the RCRBs of the same factor. This can easily be derived analytically for x_C and y_C by considering the results of Proposition 2. It holds for z_C as well, as shown in Figs. 7a–7b. The same dependence on λ was already observed in [7] assuming full knowledge of the source current distribution.

Finally, in Fig. 8 we compare the RCRBs with those obtained from (35) in Remark 1, which, under Assumption 4, reduces to

$$E = \chi \frac{e^{-jkr}}{r^{5/2}} \sqrt{x_C [x_C^2 + (y - y_C)^2]}. \quad (85)$$

Only marginal differences can be observed between the RCRBs for values of L of practical interest. However, different limits are achieved as L increases. In conclusion, both are accurate and might be used to predict scaling behaviors, but the proposed one is needed to study the fundamental limits.

VI. CONCLUSIONS

Large antenna arrays and high frequencies push towards the regime in which the impinging wavefront is no longer planar

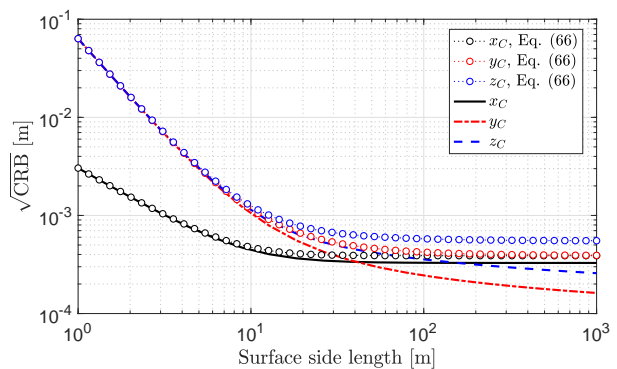


Fig. 8: Comparisons with the RCRBs for the scalar model (85) as obtained from Remark 1 under Assumption 4.

but spherical. This opens up opportunities for new signal processing algorithms for positioning. Motivated by the need of establishing ultimate bounds, we provided a general model for the electric vector field over a rectangular spatial region. Unlike standard models in signal processing, the functional dependence on the radiation vector at the source was taken into account. The electric vector field model was used to compute the CRBs for the three-dimensional (3D) spatial location of a Hertzian dipole, with and without a priori knowledge of its orientation. Further simplifications and insights were obtained by assuming that the dipole center is located on the line perpendicular to the surface center. Numerical results showed that a centimeter-level accuracy can be achieved in the near-field of surfaces of practical size (i.e., in the range of a few meters) in the mmWave and sub-THz bands. Asymptotic expressions were also given in closed-form to show the scaling behaviors with respect to surface area and wavelength.

APPENDIX A

We compute the derivatives of the cartesian components of the electric field with respect to the unknown parameters $(t_x, t_y, t_z, x_C, y_C, z_C)$. Starting from (45)–(47), after lengthy but standard calculations we have

$$\frac{\partial e_\alpha}{\partial t_\beta} = -j\chi \frac{e^{-jkr}}{r} \cdot \begin{cases} 1 - r_\alpha^2 & \text{per } \beta = \alpha, \\ -r_\alpha r_\beta & \text{per } \beta \neq \alpha \end{cases} \quad (86)$$

with $\alpha, \beta \in \{x, y, z\}$ and r_α being defined in (49),

$$\frac{\partial e_x}{\partial x_C} = \frac{-j\chi e^{-jkr}}{r^4} \left\{ jk\bar{x} [t_x(\bar{y}^2 + \bar{z}^2) - \bar{x}(t_y\bar{y} + t_z\bar{z})] + \frac{3t_x\bar{x}(\bar{y}^2 + \bar{z}^2) - (t_y\bar{y} + t_z\bar{z})(2\bar{x}^2 - \bar{y}^2 - \bar{z}^2)}{r} \right\} \quad (87a)$$

$$\frac{\partial e_x}{\partial y_C} = \frac{-j\chi e^{-jkr}}{r^4} \left\{ jk\bar{y} [t_x(\bar{y}^2 + \bar{z}^2) - \bar{x}(t_y\bar{y} + t_z\bar{z})] + \frac{t_x\bar{y}(2\bar{x}^2 - \bar{y}^2 - \bar{z}^2) - t_y\bar{x}(\bar{x}^2 - 2\bar{y}^2 + \bar{z}^2) + 3t_z\bar{x}\bar{y}\bar{z}}{r} \right\} \quad (87b)$$

$$\frac{\partial e_x}{\partial z_C} = \frac{-j\chi e^{-jkr}}{r^4} \left\{ jk\bar{z} [t_x(\bar{y}^2 + \bar{z}^2) - \bar{x}(t_y\bar{y} + t_z\bar{z})] \right. \\ \left. - \frac{t_x\bar{z}(2\bar{x}^2 - \bar{y}^2 - \bar{z}^2) + 3t_y\bar{x}\bar{y}\bar{z} - t_z\bar{x}(\bar{x}^2 + \bar{y}^2 - 2\bar{z}^2)}{r} \right\} \quad (87c)$$

$$\frac{\partial e_y}{\partial x_C} = \frac{-j\chi e^{-jkr}}{r^4} \left\{ jk\bar{x} [t_y(\bar{x}^2 + \bar{z}^2) - \bar{y}(t_x\bar{x} + t_z\bar{z})] \right. \\ \left. - \frac{t_y\bar{x}(2\bar{y}^2 - \bar{x}^2 - \bar{z}^2) - t_x\bar{y}(\bar{y}^2 - 2\bar{x}^2 + \bar{z}^2) + 3t_z\bar{x}\bar{y}\bar{z}}{r} \right\} \quad (88a)$$

$$\frac{\partial e_y}{\partial y_C} = \frac{-j\chi e^{-jkr}}{r^4} \left\{ jk\bar{y} [t_x(\bar{x}^2 + \bar{z}^2) - \bar{y}(t_x\bar{x} + t_z\bar{z})] \right. \\ \left. + \frac{3t_y\bar{y}(\bar{x}^2 + \bar{z}^2) - (t_x\bar{x} + t_z\bar{z})(2\bar{y}^2 - \bar{x}^2 - \bar{z}^2)}{r} \right\} \quad (88b)$$

$$\frac{\partial e_y}{\partial z_C} = \frac{-j\chi e^{-jkr}}{r^4} \left\{ jk\bar{z} [t_y(\bar{x}^2 + \bar{z}^2) - \bar{y}(t_x\bar{x} + t_z\bar{z})] \right. \\ \left. - \frac{t_y\bar{z}(2\bar{y}^2 - \bar{x}^2 - \bar{z}^2) + 3t_x\bar{x}\bar{y}\bar{z} - t_z\bar{y}(\bar{x}^2 + \bar{y}^2 - 2\bar{z}^2)}{r} \right\} \quad (88c)$$

$$\frac{\partial e_z}{\partial x_C} = \frac{-j\chi e^{-jkr}}{r^4} \left\{ jk\bar{x} [t_z(\bar{x}^2 + \bar{y}^2) - \bar{z}(t_x\bar{x} + t_y\bar{y})] \right. \\ \left. - \frac{t_x\bar{z}(2\bar{z}^2 - \bar{x}^2 - \bar{y}^2) + 3t_y\bar{x}\bar{y}\bar{z} - t_z\bar{z}(\bar{z}^2 + \bar{y}^2 - 2\bar{x}^2)}{r} \right\} \quad (89a)$$

$$\frac{\partial e_z}{\partial y_C} = \frac{-j\chi e^{-jkr}}{r^4} \left\{ jk\bar{y} [t_z(\bar{x}^2 + \bar{y}^2) - \bar{z}(t_x\bar{x} + t_y\bar{y})] \right. \\ \left. - \frac{t_z\bar{y}(2\bar{z}^2 - \bar{x}^2 - \bar{y}^2) - t_y\bar{z}(\bar{z}^2 - 2\bar{y}^2 + \bar{x}^2) + 3t_x\bar{x}\bar{y}\bar{z}}{r} \right\} \quad (89b)$$

$$\frac{\partial e_z}{\partial z_C} = \frac{-j\chi e^{-jkr}}{r^4} \left\{ jk\bar{z} [t_z(\bar{x}^2 + \bar{y}^2) - \bar{z}(t_x\bar{x} + t_y\bar{y})] \right. \\ \left. + \frac{3t_z\bar{z}(\bar{x}^2 + \bar{y}^2) - (t_x\bar{x} + t_y\bar{y})(2\bar{z}^2 - \bar{y}^2 - \bar{x}^2)}{r} \right\}. \quad (89c)$$

For convenience, we have set $\bar{x} = -x_C$, $\bar{y} = y - y_C$ e $\bar{z} = z - z_C$.

APPENDIX B

In this appendix, we prove the results of Proposition 1. We start by observing that, under Assumption 4, the derivatives needed for the computation of FIM in (51) are obtained from the equations in Appendix A by simply setting $y_C = z_C = 0$, $t_x = t_y = 0$ and $t_z = 1$.

We consider first the computation of \mathbf{F}_{cc} whose elements are given by

$$[\mathbf{F}_{cc}]_{mn} = \frac{1}{\sigma^2} \int_{-\frac{L}{2}}^{\frac{L}{2}} \int_{-\frac{L}{2}}^{\frac{L}{2}} f_{mn}^{(cc)}(y, z) dy dz \quad (90)$$

where

$$f_{mn}^{(cc)}(y, z) = \frac{\partial e_x(\mathbf{r})}{\partial a_m} \frac{\partial e_x^*(\mathbf{r})}{\partial a_n} + \frac{\partial e_y(\mathbf{r})}{\partial a_m} \frac{\partial e_y^*(\mathbf{r})}{\partial a_n} + \frac{\partial e_z(\mathbf{r})}{\partial a_m} \frac{\partial e_z^*(\mathbf{r})}{\partial a_n} \quad (91)$$

with $a_1 = x_C$, $a_2 = y_C$ and $a_3 = z_C$. In this case, it can be shown that, for $m \neq n$, $f_{mn}^{(cc)}(y, z)$ in (91) is an odd function of y and z , i.e.,

$$f_{mn}^{(cc)}(y, z) = -f_{mn}^{(cc)}(-y, z) = -f_{mn}^{(cc)}(y, -z).$$

As a result, due to the symmetry of the integration domain, the off-diagonal elements of \mathbf{F}_{cc} are zero, meaning that \mathbf{F}_{cc} is a diagonal matrix. As for the diagonal elements, standard but lengthy calculations show that they can be written as in (65)–(67) where

$$\mathcal{J}_1 \triangleq \frac{\rho}{2(1+\rho^2)} \left[\frac{(7+6\rho^2)}{\sqrt{1+\rho^2}} \arctan \frac{\rho}{\sqrt{1+\rho^2}} + \frac{\rho}{(1+2\rho^2)} \right] \quad (92)$$

$$\mathcal{J}_2 \triangleq \int_{-\rho/2}^{\rho/2} \int_{-\rho/2}^{\rho/2} \frac{1+u^2v^2+v^4}{(1+u^2+v^2)^4} dudv \quad (93)$$

$$\mathcal{J}_3 \triangleq \int_{-\rho/2}^{\rho/2} \int_{-\rho/2}^{\rho/2} \frac{u^2(1+u^2)}{(1+u^2+v^2)^3} dudv \quad (94)$$

$$\mathcal{J}_4 \triangleq \int_{-\rho/2}^{\rho/2} \int_{-\rho/2}^{\rho/2} \frac{u^2(1+u^2) + v^2(1+v^2) - u^2v^2}{(1+u^2+v^2)^4} dudv \quad (95)$$

$$\mathcal{J}_5 \triangleq \int_{-\rho/2}^{\rho/2} \int_{-\rho/2}^{\rho/2} \frac{v^2(1+u^2)}{(1+u^2+v^2)^3} dudv \quad (96)$$

$$\mathcal{J}_6 \triangleq \left[\frac{\rho(18\rho^4 + 38\rho^2 + 17)}{4(1+\rho^2)^{5/2}} \arctan \left(\frac{\rho}{\sqrt{\rho^2+1}} \right) \right. \\ \left. + \frac{\rho^2(6\rho^4 + 2\rho^2 - 1)}{4(1+\rho^2)^2(1+2\rho^2)^2} \right] \quad (97)$$

with $\rho = L/x_C$. Now, we consider the computation of \mathbf{F}_{tt} whose elements are given by

$$[\mathbf{F}_{tt}]_{mn} = \frac{1}{\sigma^2} \int_{-\frac{L}{2}}^{\frac{L}{2}} \int_{-\frac{L}{2}}^{\frac{L}{2}} f_{mn}^{(tt)}(y, z) dy dz \quad (98)$$

where

$$f_{mn}^{(tt)}(y, z) = \frac{\partial e_x(\mathbf{r})}{\partial b_m} \frac{\partial e_x^*(\mathbf{r})}{\partial b_n} + \frac{\partial e_y(\mathbf{r})}{\partial b_m} \frac{\partial e_y^*(\mathbf{r})}{\partial b_n} + \frac{\partial e_z(\mathbf{r})}{\partial b_m} \frac{\partial e_z^*(\mathbf{r})}{\partial b_n} \quad (99)$$

with $b_1 = t_x$, $b_2 = t_y$ and $b_3 = t_z$. Again, it can easily be shown that, for $m \neq n$, $f_{mn}^{(tt)}(y, z)$ in (99) is an odd function of y or z , and hence the off-diagonal elements of \mathbf{F}_{tt} are zero,

meaning that \mathbf{F}_{tt} is diagonal. The diagonal elements can be written as in (68)–(69) where

$$\mathcal{J}_7 \triangleq \int_{-\rho/2}^{\rho/2} \int_{-\rho/2}^{\rho/2} \frac{u^2 + v^2}{(1 + u^2 + v^2)^2} dudv \quad (100)$$

$$\mathcal{J}_8 \triangleq \int_{-\rho/2}^{\rho/2} \int_{-\rho/2}^{\rho/2} \frac{1 + u^2}{(1 + u^2 + v^2)^2} dudv. \quad (101)$$

Consider now the matrix \mathbf{F}_{tc} whose elements are given by

$$[\mathbf{F}_{tc}]_{mn} = \frac{1}{\sigma^2} \int_{-\frac{\lambda}{2}}^{\frac{\lambda}{2}} \int_{-\frac{\lambda}{2}}^{\frac{\lambda}{2}} f_{mn}^{(tc)}(y, z) dydz \quad (102)$$

where

$$f_{mn}^{(tc)}(y, z) = \frac{\partial e_x(\mathbf{r})}{\partial b_m} \frac{\partial e_x^*(\mathbf{r})}{\partial a_n} + \frac{\partial e_y(\mathbf{r})}{\partial b_m} \frac{\partial e_y^*(\mathbf{r})}{\partial a_n} + \frac{\partial e_z(\mathbf{r})}{\partial b_m} \frac{\partial e_z^*(\mathbf{r})}{\partial a_n} \quad (103)$$

and a_n, b_m have the same meaning as before. It can be shown that $f_{13}^{(tc)}(y, z)$ and $f_{31}^{(tc)}(y, z)$ are even functions of y or z whereas the others are odd functions of y or z . As a consequence, the only non-zero entries are $[\mathbf{F}_{tc}]_{13}$ and $[\mathbf{F}_{tc}]_{31}$ whose expressions are given by (70) and (71) where

$$\mathcal{J}_9 \triangleq \frac{-4j}{3} \left[\arctan \frac{\rho^2}{\sqrt{1+2\rho^2}} - \frac{\rho^2}{(1+\rho^2)\sqrt{1+2\rho^2}} \right] \quad (104)$$

$$\mathcal{J}_{10} \triangleq j \int_{-\rho/2}^{\rho/2} \int_{-\rho/2}^{\rho/2} \frac{(1+u^2)}{(1+u^2+v^2)^{5/2}} dudv \quad (105)$$

$$\mathcal{J}_{11} \triangleq - \int_{-\rho/2}^{\rho/2} \int_{-\rho/2}^{\rho/2} \frac{1}{(1+u^2+v^2)^3} dudv. \quad (106)$$

APPENDIX C

The proof of Proposition 2 is given. We start by deriving (78) and (80). As a first step, we show that $k^2\mathcal{J}_1 \gg x_C^{-2}\mathcal{J}_2$, for $x_C \gg \lambda$. To this end, observe that \mathcal{J}_1 results from the following integral

$$\mathcal{J}_1 = \int_{-\rho/2}^{\rho/2} \int_{-\rho/2}^{\rho/2} \frac{1+v^2}{(1+u^2+v^2)^3} dudv, \quad (107)$$

Comparing (107) and (93) yields $\mathcal{J}_1 > \mathcal{J}_2$ since

$$\frac{1+v^2}{(1+u^2+v^2)^3} \geq \frac{1+u^2v^2+v^4}{(1+u^2+v^2)^4}. \quad (108)$$

Accordingly, we have that

$$4\pi^2\lambda^{-2}\mathcal{J}_1 \gg x_C^{-2}\mathcal{J}_2 \quad (109)$$

for $x_C \gg \lambda$. The approximation in (80) derives from (109) immediately. Now, we show that $k|\mathcal{J}_{10}| \gg x_C^{-1}|\mathcal{J}_{11}|$. Since

$$\frac{(1+u^2)}{(1+u^2+v^2)^{5/2}} \geq \frac{1}{(1+u^2+v^2)^3}$$

from (105) and (106) it follows that $|\mathcal{J}_{10}| > |\mathcal{J}_{11}|$, and thus

$$2\pi^2\lambda^{-1}|\mathcal{J}_{10}| \gg x_C^{-1}|\mathcal{J}_{11}| \quad (110)$$

for $x_C \gg \lambda$. Accordingly, $|k\mathcal{J}_{10} + x_C^{-1}\mathcal{J}_{11}|^2 \approx k^2|\mathcal{J}_{10}|^2$ which, together with (109), yields (78).

We now derive (79) by showing that $k^2\mathcal{J}_3 \gg x_C^{-2}\mathcal{J}_4$. Observe that

$$0 < \mathcal{J}_4 < \int_{-\rho/2}^{\rho/2} \int_{-\rho/2}^{\rho/2} \frac{2u^2(1+u^2)}{(1+u^2+v^2)^4} dudv < 2\mathcal{J}_3 \quad (111)$$

from which we easily obtain

$$4\pi^2\lambda^{-2}\mathcal{J}_3 \gg x_C^{-2}\mathcal{J}_4 \quad (112)$$

for $x_C \gg \lambda$. The approximation in (79) follows from (112) immediately.

APPENDIX D

The analysis of the CRBs in the asymptotic regime $\rho \rightarrow \infty$ requires the computation of the following limits

- 1) $\lim_{\rho \rightarrow \infty} (\mathcal{J}_1 - \mathcal{J}_8^{-1} |\mathcal{J}_{10}|^2)$
- 2) $\lim_{\rho \rightarrow \infty} \mathcal{J}_3$
- 3) $\lim_{\rho \rightarrow \infty} \left[k^2 (\mathcal{J}_5 - \mathcal{J}_7^{-1} |\mathcal{J}_9|^2) + x_C^{-2} \mathcal{J}_6 \right]$.

We start by evaluating the first. From (92), we have

$$\lim_{\rho \rightarrow \infty} \mathcal{J}_1 = 3\pi/4. \quad (113)$$

As for the ratio $|\mathcal{J}_{10}|^2/\mathcal{J}_8$, we observe that

$$\mathcal{J}_8 \stackrel{(a)}{>} \int_{\mathcal{C}^-} \frac{1+u^2}{(1+u^2+v^2)^2} dudv \quad (114)$$

$$= \frac{\pi}{2} [\ln(1+\rho^2/4) + \rho^2/(\rho^2+4)] \quad (115)$$

and

$$|\mathcal{J}_{10}| \stackrel{(b)}{<} \int_{\mathcal{C}^+} \frac{1+u^2}{(1+u^2+v^2)^{5/2}} dudv \quad (116)$$

$$= \frac{4\pi}{3} \frac{\rho^4 - \sqrt{\frac{\rho^2+2}{2}} \left(\frac{3\rho^2+8}{2} \right) + 4(\rho^2+1)}{(\rho^2+2)^2} \quad (117)$$

where (a) and (b) follow by replacing the squared integration domain $\mathcal{D} = \{(u, v) | -\rho/2 \leq u, v \leq \rho/2\}$, respectively, with the two circular domains, $\mathcal{C}^- = \{(u, v) | u^2 + v^2 \leq \rho/2\}$ and $\mathcal{C}^+ = \{(u, v) | u^2 + v^2 \leq \sqrt{2}\rho/2\}$. Based on (115) and (117), it is easily shown that

$$\lim_{\rho \rightarrow \infty} \mathcal{J}_8^{-1} |\mathcal{J}_{10}|^2 = 0. \quad (118)$$

Taking (113) and (118) into account yields (82).

Consider now \mathcal{J}_3 . Due to the non-negativity of the function $u^2(1+u^2)/(1+u^2+v^2)^3$, we have

$$\int_{\mathcal{C}^-} \frac{u^2(1+u^2)}{(1+u^2+v^2)^3} dudv < \mathcal{J}_3 < \int_{\mathcal{C}^+} \frac{u^2(1+u^2)}{(1+u^2+v^2)^3} dudv \quad (119)$$

The two integrals can be computed in closed form. In particular, we obtain

$$\int_{c^-} \frac{u^2(1+u^2)}{(1+u^2+v^2)^3} dudv = \frac{3\pi}{8} \ln(1+\rho^2) - \frac{\pi}{16} \frac{\rho^2(5\rho^2+6)}{(1+\rho^2)^2} \quad (120)$$

$$\int_{c^+} \frac{u^2(1+u^2)}{(1+u^2+v^2)^3} dudv = \frac{3\pi}{8} \ln(1+2\rho^2) - \frac{\pi}{4} \frac{\rho^2(5\rho^2+3)}{(1+2\rho^2)^2}. \quad (121)$$

Taking (119) and (120)–(121) into account yields

$$\mathcal{J}_3 \sim \frac{3\pi}{4} \ln \rho \quad \text{as } \rho \rightarrow \infty \quad (122)$$

from which (83) is derived straightforwardly.

Finally, we focus on the limit

$$\lim_{\rho \rightarrow \infty} \left[k^2 \left(\mathcal{J}_5 - \mathcal{J}_7^{-1} |\mathcal{J}_9|^2 \right) + x_C^{-2} \mathcal{J}_6 \right] \quad (123)$$

and start from \mathcal{J}_5 . By using similar arguments to those for \mathcal{J}_3 , it can be shown that

$$\mathcal{J}_5 \sim \frac{\pi}{4} \ln \rho \quad \text{as } \rho \rightarrow \infty. \quad (124)$$

As for the ratio $|\mathcal{J}_9|^2/\mathcal{J}_7$, similarly to (115) we can write

$$\mathcal{J}_7 > \int_{c^-} \frac{u^2+v^2}{(1+u^2+v^2)^2} dudv \quad (125)$$

$$= \pi \left[\ln(1+\rho^2/4) - \rho^2/(\rho^2+4) \right] \quad (126)$$

whereas from (104) we obtain

$$\lim_{\rho \rightarrow \infty} \mathcal{J}_9 = -j2\pi/3. \quad (127)$$

This means that

$$\lim_{\rho \rightarrow \infty} \mathcal{J}_7^{-1} |\mathcal{J}_9|^2 = 0. \quad (128)$$

As for \mathcal{J}_6 , from (97) we have

$$\lim_{\rho \rightarrow \infty} \mathcal{J}_6 = 9\pi/8. \quad (129)$$

Taking (124), (128) and (129) into account, (84) follows easily.

REFERENCES

- [1] A. D. J. Torres, A. A. D’Amico, L. Sanguinetti, and M. Z. Win, “Cramér-Rao bounds for near-field localization,” in *Asilomar Conference on Signals, Systems, and Computers*, 2021. [Online]. Available: <https://arxiv.org/abs/2104.14825>
- [2] J. Lee, E. Tejedor, K. Ranta-aho, H. Wang, K. T. Lee, E. Semaan, E. Mohyeldin, J. Song, C. Bergljung, and S. Jung, “Spectrum for 5G: Global status, challenges, and enabling technologies,” *IEEE Commun. Mag.*, vol. 56, no. 3, pp. 12–18, 2018.
- [3] C. Huang, S. Hu, G. C. Alexandropoulos, A. Zappone, C. Yuen, R. Zhang, M. D. Renzo, and M. Debbah, “Holographic MIMO surfaces for 6G wireless networks: Opportunities, challenges, and trends,” *IEEE Wireless Communications*, vol. 27, no. 5, pp. 118–125, 2020.
- [4] A. Pizzo, T. L. Marzetta, and L. Sanguinetti, “Spatially-stationary model for Holographic MIMO small-scale fading,” *IEEE J. Sel. Areas Commun.*, vol. 38, no. 9, pp. 1964–1979, 2020.
- [5] “Holographic communication using intelligent surfaces,” *IEEE Commun. Mag.*, vol. 59, no. 6, pp. 35–41, 2021.
- [6] S. Hu, F. Rusek, and O. Edfors, “Beyond massive MIMO: The potential of data transmission with large intelligent surfaces,” vol. 66, no. 10, pp. 2746–2758, 2018.
- [7] —, “Beyond massive MIMO: The potential of positioning with large intelligent surfaces,” *IEEE Trans. Signal Process.*, vol. 66, no. 7, pp. 1761–1774, 2018.
- [8] E. Basar, M. Di Renzo, J. De Rosny, M. Debbah, M. Alouini, and R. Zhang, “Wireless communications through reconfigurable intelligent surfaces,” *IEEE Access*, vol. 7, pp. 116 753–116 773, 2019.
- [9] M. Di Renzo, A. Zappone, M. Debbah, M. S. Alouini, C. Yuen, J. de Rosny, and S. Tretyakov, “Smart radio environments empowered by reconfigurable intelligent surfaces: How it works, state of research, and the road ahead,” *IEEE J. Sel. Areas Commun.*, vol. 38, no. 11, pp. 2450–2525, 2020.
- [10] A. Bourdoux, A. N. Barreto, B. van Liempd, C. de Lima, D. Dardari, D. Belot, E.-S. Lohan, G. Seco-Granados, H. Srieddeen, H. Wymeersch, J. Suutala, J. Saloranta, M. Guillaud, M. Isomursu, M. Valkama, M. R. K. Aziz, R. Berkvens, T. Sanguanpuak, T. Svensson, and Y. Miao, “6G white paper on localization and sensing,” 2020. [Online]. Available: <https://arxiv.org/abs/2006.01779>
- [11] B. Friedlander, “Localization of signals in the near-field of an antenna array,” *IEEE Trans. Signal Process.*, vol. 67, no. 15, pp. 3885–3893, 2019.
- [12] J.-S. Jiang and M. Ingram, “Spherical-wave model for short-range MIMO,” *IEEE Trans. Commun.*, vol. 53, no. 9, pp. 1534–1541, 2005.
- [13] F. Bohagen, P. Orten, and G. E. Oien, “On spherical vs. plane wave modeling of line-of-sight MIMO channels,” *IEEE Trans. Commun.*, vol. 57, no. 3, pp. 841–849, 2009.
- [14] J. Yang, Y. Zeng, S. Jin, C. K. Wen, and P. Xu, “Communication and localization with extremely large lens antenna array,” *IEEE Transactions on Wireless Communications*, pp. 1–1, 2021.
- [15] J. V. Alegria and F. Rusek, “Cramér-Rao lower bounds for positioning with large intelligent surfaces using quantized amplitude and phase,” in *Asilomar Conference on Signals, Systems, and Computers*, 2019, pp. 10–14.
- [16] F. Guidi and D. Dardari, “Radio positioning with EM processing of the spherical wavefront,” *IEEE Trans. Wireless Commun.*, vol. 20, no. 6, pp. 3571–3586, 2021.
- [17] J. P. Delmas, M. N. El Korso, H. Gazzah, and M. Castella, “CRB analysis of planar antenna arrays for optimizing near-field source localization,” *Signal Process.*, vol. 127, pp. 117–134, 2016. [Online]. Available: <https://www.sciencedirect.com/science/article/pii/S0165168416000815>
- [18] J.-P. Le Cadre, “Performance analysis of wavefront curvature methods for range estimation of a moving source,” *IEEE Trans. Aerosp. Electron. Syst.*, vol. 31, no. 3, pp. 1082–1103, 1995.
- [19] E. Grosicki, K. Abed-Meraim, and Y. Hua, “A weighted linear prediction method for near-field source localization,” *IEEE Trans. Signal Process.*, vol. 53, no. 10, pp. 3651–3660, 2005.
- [20] M. N. El Korso, A. Renaux, R. Boyer, and S. Marcos, “Deterministic performance bounds on the mean square error for near field source localization,” *IEEE Trans. Signal Process.*, vol. 61, no. 4, pp. 871–877, 2013.
- [21] S. Zhang, T. Jost, R. Pöhlmann, A. Dammann, D. Shutin, and P. A. Hoeher, “Spherical wave positioning based on curvature of arrival by an antenna array,” *IEEE Wireless Commun. Lett.*, vol. 8, no. 2, pp. 504–507, 2019.
- [22] X. Yin, S. Wang, N. Zhang, and B. Ai, “Scatterer localization using large-scale antenna arrays based on a spherical wave-front parametric model,” *IEEE Trans. Wireless Commun.*, vol. 16, no. 10, pp. 6543–6556, 2017.
- [23] A. Guerra, F. Guidi, D. Dardari, and P. M. Djuric, “Near-field tracking with large antenna arrays: Fundamental limits and practical algorithms,” *IEEE Trans. Signal Process.*, pp. 1–1, 2021.
- [24] W. C. Chew, *Waves and Fields in Inhomogeneous Media*. Wiley-IEEE Press, 1995.
- [25] S. J. Orfanidis, *Electromagnetic Waves and Antennas*. [Online]. Available: <http://www.ece.rutgers.edu/orfanidi/ewal>, 2008.
- [26] M. A. Jensen and J. W. Wallace, “Capacity of the continuous-space electromagnetic channel,” *IEEE Trans. Antennas Propag.*, vol. 56, no. 2, pp. 524–531, 2008.
- [27] F. K. Gruber and E. A. Marengo, “New aspects of electromagnetic information theory for wireless and antenna systems,” *IEEE Transactions on Antennas and Propagation*, vol. 56, no. 11, pp. 3470–3484, 2008.
- [28] S. M. Kay, *Fundamentals of statistical signal processing: Estimation theory*. Prentice Hall, 1993.
- [29] K. Witrissal, P. Meissner, E. Leitinger, Y. Shen, C. Gustafson, F. Tufveson, K. Haneda, D. Dardari, A. Molisch, A. Conti, and M. Win, “High-accuracy localization for assisted living: 5G systems will turn multipath channels from foe to friend,” *IEEE Signal Process. Mag.*, vol. 33, pp. 59–70, 03 2016.